BIOCHEMISTRY

 Volume 47, Number 46 November 18, 2008

Articles

NMR Solution Structures of Bistranded Abasic Site Lesions in DNA[†,‡]

Raphael D. Hazel,[§] Kegui Tian,[||] and Carlos de los Santos*[,||]

Department of Physiology & Biophysics, and Department of Pharmacological Sciences, Stony Brook University, School of Medicine, Stony Brook, New York 11794-8651

Received May 20, 2008; Revised Manuscript Received September 17, 2008

ABSTRACT: Ionizing radiation produces clustered lesions in DNA. Since the orientation of bistranded lesions affects their recognition by DNA repair enzymes, clustered damages are more difficult to process and thus more toxic than single oxidative lesions. In order to understand the structural determinants that lead to differential recognition, we used NMR spectroscopy and restrained molecular dynamics to solve the structure of two DNA duplexes, each containing two stable abasic site analogues positioned on opposite strands of the duplex and staggered in the 3′ (−1 duplex, $(AP)_2$−1 duplex) or 5′ (+1 duplex, $(AP)_2$+1 duplex) direction. Cross-peak connectivities observed in the nonexchangeable NOESY spectra indicate compression of the helix at the lesion site of the duplexes, resulting in the formation of two abasic bulges. The exchangeable proton spectra show the AP site partner nucleotides forming interstrand hydrogen bonds that are characteristic of a Watson−Crick G•C base pairs, confirming the extra helical nature of the AP residues. Restrained molecular dynamics simulations generate a set of converging structures in full agreement with the spectroscopic data. In the $(AP)_2$−1 duplex, the extra helical abasic site residues reside in the minor groove of the helix, while they appear in the major groove in the $(AP)_2$+1 duplex. These structural differences are consistent with the differential recognition of bistranded abasic site lesions by human AP endonuclease.

Ionizing radiation causes oxidative DNA damage in the cells producing various types of base damages, strand breaks, and abasic sites (AP sites). In an aqueous environment, DNA damages are indirect, resulting from the reaction with hydroxyl free radicals induced by radiation *1, 3*). Since a single energy deposition event can form several hydroxyl radicals, ionizing radiation has the potential to produce clustered DNA damages, defined as two or more lesions within one turn of the DNA helix (*1, 4, 5*). Repair of clustered lesions can have different cellular outcomes including the generation of toxic double strand breaks (DSBs), lesions that form the basis for the utilization of ionizing radiation in cancer therapy. However, they are highly mutagenic when left unrepaired.

Base excision repair (BER) of AP lesions starts when a DNA glycosylase with $\beta-\delta$ elimination activity removes the abasic nucleotide, or after an AP endonuclease incises the phosphodiester bond at the 5′-side of the lesion (*6*−*8*). However, the repair of clustered AP lesions, as well as that of multiple DNA damage sites in general, are more complex and can elicit different outcomes. Deletion mutants for the three major DNA glycosylases in *E. coli*, which leaves

[†] This study was supported NIH grants CA77094 and CA47995.

[‡] Atomic coordinates were deposited in the RCSB Protein Data Bank: ID codes 1YCW and 1YCT for the $(AP)_2$−1 duplex and the $(AP)_2$+1 duplex, respectively.

* Corresponding author. Phone: (631) 444-3649. Fax: (631) 444-3218. E-mail: cds@pharm.sunysb.edu.

[§] Department of Physiology & Biophysics.

[||] Department of Pharmacological Sciences.

10.1021/bi800950t CCC: $40.75
Published on Web 10/25/2008

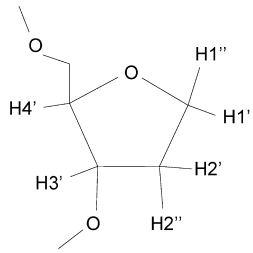

3-hydroxy-4-hydroxymethyl-tetrahydrofuran (F)

C1 G2 C3 A4 T5 G6 **F7** G8 T9 A10 C11 G12 C13
G26 C25 G24 T23 A22 **F21** C20 C19 A18 T17 G16 C15 G14

$(AP)_2$–1 Duplex

C1 G2 C3 A4 T5 G6 **F7** G8 T9 A10 C11 G12 C13
G26 C25 G24 T23 A22 C21 C20 **F19** A18 T17 G16 C15 G14

$(AP)_2$+1 Duplex

FIGURE 1: Chemical structure of the tetrahydrofuran AP residue and DNA sequences of the $(AP)_2-1$ and the $(AP)_2+1$ duplexes. Signs indicate the relative orientation of the second AP site being negative when positioned toward the 5′-side of the first (reference) lesion.

bacteria unable to remove oxidized bases, show greater survival rates and a lower number of DSBs after exposure to ionizing radiation than wild type cells (*9*). Human hematopoietic cells can efficiently join DSBs within 24 h after irradiation, but the number of bistranded abasic sites clusters decreases very slowly over a 14 day period (*10*).

In vitro, inhibition of DNA incision occurs with both bacterial and mammalian proteins when the bistranded lesions are up to five base pairs away (*11*−*13*). *E. coli* formamidopyrimidine DNA glycosylase (Fpg) can remove an 8-oxo-dG lesion or an AP site positioned 3 or 6 base pairs away from a single strand break in the opposing strand. However, incision is less efficient when the clustered lesions are staggered in the +1 or −1 orientation (*13*) (see Figure 1 for the sign convention used throughout this article). Clustered lesions also affect the efficiency of mammalian BER proteins (*10, 14*−*18*). Human AP endonuclease 1 (hApe1) incises +1 and +3 bistranded $(AP)_2$ substrates less efficiently than a single AP duplex, but does it still reasonably well. In contrast, it shows greatly reduced activity processing −1 and −3 $(AP)_2$ clusters (*11*) and is only 30% active with two directly opposed AP lesions (*18*). Furthermore, human cell extracts from mononuclear blood cells can efficiently cleave bistranded abasic lesions separated by five base pairs or more, irrespective of their orientation, but respond somewhat poorly with closely spaced lesions, especially on clusters staggered in the 5′ direction (*10*). This differential recognition fades with increased separation between the lesions, and bistranded $(AP)_2$ sites located six or more nucleotides apart behave as single AP lesions.

The structural determinants that affect BER recognition of bistranded $(AP)_2$ sites are not understood. Many research groups have investigated the structures of short DNA duplexes having a single of abasic site (natural, oxidized, reduced, or the stable THF analogue) placed opposite to a purine (apyrimidinic site), a pyrimidine (apurinic site), or in the context of a single base deletion (*19*−*33*). In all cases, the helix remains right-handed with the AP residue stacked inside the helix or looped out depending on the temperature, sequence context, and the nature of the opposing base. When the orphan base is a purine, both the AP site strand its partner residue remained stacked inside the helix with backbone perturbations occurring on the lesion site and adjacent base pairs (*19*−*21, 25*−*31*). However, when the abasic site is located in an A-tract in which case the disturbance extends over several base pairs at either side of the lesion (*25*). On the other hand, apurinic sites and sometimes the pyrimidine counter residue can be extra helical, depending on the temperature and duplex sequence context (*21, 23, 26, 27*).

Previously, we reported the solution structure of DNA containing a $(AP)_2-1$ or $(AP)_2+1$ cluster observing the extrusion of the AP residues in both clusters, with the formation of a novel G•A mismatch only in the −1 orientation (*34*). In order to address the role of duplex sequence, we established the solution structure of two DNA duplexes containing a bistranded $(AP)_2-1$ or $(AP)_2+1$ cluster, with dC and dG pairing the abasic residues, as determined by NMR spectroscopy and restrained molecular dynamics simulations. Figure 1 shows the sequence of $(AP)_2$ duplexes and the chemical structure of tetrahydrofuran, the abasic site analogue used in this study.

MATERIALS AND METHODS

Oligonucleotide Synthesis and Duplex Preparation. The synthesis of AP containing duplexes was done using standard phosphoramidite chemistry procedures with commercial reagents purchased from Glen Research Corporation. Samples purification was accomplished by two runs of reverse phase HPLC, using a C18 column as previously reported (*34*). Conversion of the samples to their sodium salt was achieved by running then through a Sephadex G-25 column followed by a Dowex 50W ion-exchange resin. The concentration of oligomeric DNA was determined by UV_{260} absorption using extension coefficients calculated by Generunner (V3.0, Hasting Software, Inc.). Complementary strands were annealed by heating the samples to 80 °C and slowly cooling to room temperature. Samples were then lyophilized and dissolved in 0.7 mL of 25 mM phosphate buffer at pH 6.8, containing 50 mM NaCl and 0.5 mM EDTA in 99.96% D_2O (D_2O buffer) or in 90% H_2O/10% D_2O (H_2O buffer). DNA concentration of samples used for NMR spectroscopy was about 2 mM.

Duplex samples used for the hApe1 incision studies were prepared as described above. The samples consisted of 36-mer duplexes containing the bistranded $(AP)_2-1$ (or $(AP)_2+1$) cluster in the same sequence context than that used for the NMR study.

NMR Methods. One- and two-dimensional NMR spectra were recorded in Varian (INOVA) spectrometers at 600 or 500 MHz field strengths. Proton spectra were collected from samples dissolved in D_2O buffer at 25 °C and in H_2O buffer at 1 °C. Proton chemical shifts were referenced to external 3-(trimethylsilyl)-propionate-2,2,3,3,-d_4 at 0 ppm (ppm). Phase-sensitive NOESY (*35*), COSY, COSY45, DQF-COSY, and TOCSY spectra were collected for proton assignment and to aid the determination of 2′-deoxyribose conformations. Interproton distances were based on NOESY (50, 120, 190, 260, and 300 ms mixing time) spectra recorded in D_2O buffer using a repetition delay of 1.4 s. The residual water sample was suppressed by saturation pulse. TOCSY spectra were collected in D_2O buffer using isotropic mixing times of 60

and 120 ms. NOESY spectra in H_2O buffer were recorded using mixing times of 120 and 220 ms and a jump-return reading pulse (*36*). Two-dimensional data sets consisted of 2048 by 300 complex points in the t_2 and t_1 dimensions, respectively. COSY45 spectra were acquired with doubled number of complex points in both dimensions. The temperature dependence of imino protons was investigated over the 0−55 °C temperature range using 5 °C intervals. NMR spectra were processed an analyzed on Silicon Graphics workstations using FELIX98 (Accelrys, San Deigo, CA). NOESY and TOCSY time domain data were multiplied by 90°-shifted sinebell window functions. COSY, COSY45, and DQF-COSY data sets were multiplied by a sine bell function and an exponential function, using 4 Hz of line broadening. The water signal on spectra collected with the sample dissolved in 10% D_2O buffer was suppressed further by subtraction of a convolution function before Fourier transformation.

Computational Methods. Restrained molecular dynamics (rMD) simulations were run on Silicon Graphics computers using XPLOR 3.1 (*37*). Structures were visualized with InsightII (Accelrys, San Deigo, CA) and Midas Plus (UCSF, Computer Graphics Laboratory), and helical parameters were computed using Curves 5.1 (*38, 39*). Molecular dynamics were done in vacuum using an all atom force field derived from CHARM (*40*). Partial atomic charges on the phosphates were not reduced, leaving deoxynucleotide residues with a net charge of −1. Interproton distances were computed using cross-peak volume intensities measured on the 50, 120, 190, and 260 ms mixing time NOESY spectra. Each of the four NOE peak volume files was input, separately, in a relaxation protocol in XPLOR, which minimized the structure of model duplexes using only a potential energy function proportional to the difference between experimental and back calculated peak NOE intensities. Initial structures of the $(AP)_2-1$ and the $(AP)_2+1$ clusters were constructed in InsightII from canonical B-form 13-mer duplexes, containing central G·C base pairs and deleting a purine and a pyrimidine base from each strand to create the bistranded $(AP)_2$ lesions. During the relaxation protocol, duplex protons were energy minimized to fit the set of experimental NOE peak intensities that were given error bounds of 0.5%. Interproton distances were extracted from the last atom coordinates of the minimization, resulting in four interproton distance sets for each $(AP)_2$ duplex. Distance files were averaged to produce a unique interproton distance set. Interproton distances fixed by covalent-geometry, such as cytosine H5−H6 or sugar H2′-H2″, were systematically underestimated by this approach and, as a result, a correction of 20% was applied to all interproton distances. A total of 436 and 441 experimental interproton distances for the $(AP)_2-1$ and $(AP)_2+1$ duplexes, respectively, were enforced during restrained molecular dynamics simulations by using square-well potential energy functions. Distance boundaries were set to ± 0.6 Å of the average. Distances obtained from overlapped peaks had boundaries of ± 0.8 Å. Following the analysis of NOESY spectra in H_2O buffer, Watson−Crick (WC) alignments on all canonical base pairs were enforced by distance restraints with bounds of ± 0.1 Å from the values determined by X-ray crystallography. Similarly, the central G·C base pair at the lesion site was also restrained in both duplexes. Following the analysis of COSY45 spectra (*41, 42*), sugar conformations of the 4 terminal residues of the duplexes were restrained within the C2′-endo range using empirical dihedral angle square-well potential energy functions. Sugar conformations at the center of the $(AP)_2$ duplexes were restrained within the C3′-exo/C2′-endo/C1′-exo range. The SHAKE algorithm was used to maintain the length of covalent bonds involving protons (*43*). Initial models were energy minimized before beginning molecular dynamics.

Our molecular dynamics protocol consisted in slowly raising in 70 ps the temperature of the simulation from one of four starting temperatures (150, 200, 250, and 300 K) to 500 K, the high temperature value, while the scale of the penalty function enforcing distance restraints was gradually increased from 50 to 300 kcal/mol/Å^2. The system was equilibrated at 500 K for periods of 42, 44, 46, 48 and 50 ps, after which the temperature of the simulation was slowly cooled to 300 K in 40 ps, and the simulations continued by an additional 120 ps at this temperature. The four initial temperature values and the five variations in the length of the high-temperature step produced a set of 20 distance refined structures for each $(AP)_2$ duplex. Final atom coordinates underwent 1000 steps of energy minimization, generating the distance-refined models. Five refined models for each duplex showed no NOE violations >0.1 Å and exhibited pair wise root-mean-square deviations (rmsd) <1.5 Å in the atom position, comprising the family of converging structures discussed in the article.

Protein Purification. hApe1 expression and purification followed protocols described previously (*17*). BL21(DE3) pLysS bacteria, transformed with an hApe1-containing pET-28A plasmid, was grown in minimal medium to a culture density of $A_{600} = 0.9-1$, at 37 °C. At this point, addition of 1 mM IPTG and additional 6 h of incubation at the same temperature induced hApe1 expression. Bacteria were then harvested by centrifugation, suspended in 25 mM HEPES, pH 7.9, buffer containing 5 mM EDTA, 0.5 mM DTT, and 100 mM NaCl and disrupted by sonication. Subsequent, 15 min of centrifugation at 12,000 rpm (Sorvall, SS-34 rotor) at 4 °C clarified the protein extract, which was then injected in a two-column system composed of a fast flow Q-Sepharose connected to a fast flow S-Sepharose. hApe1 protein was eluted from the S-Sepharose column using a linear gradient of 0.1 to 1.5 M of NaCl over 200 mL. Fractions containing hApe1 were concentrated and loaded into a Superdex-75 column (1.6 × 60 cm, Pharmacia), pre-equilibrated with 25 mM HEPES buffer, pH 7.9, 0.5 mM EDTA, and 0.5 mM DTT and eluted using the same buffer. Purified hApe1 was run as a single band in a 12% SDS−PAGE. The Bradford protein assay (Bio-Rad, Inc.) was used to determine hApe1 concentration using bovine serum albumin as standard.

hApe1 Digestion Experiments. Duplex incision reactions were performed by duplicate in 20 μL reaction volumes, as described previously (*17*). Reaction mixtures contained 100 nM of duplex substrate and 0.03 nM of purified hApe1 dissolved in 25 mM HEPES buffer, pH 7.6, containing 50 mM NaCl, 50 mM KCl, 2 mM $MgCl_2$, 0.5 mM DTT, 6% glycerol, and 0.5 mM EDTA. Reaction mixtures stood on ice for 15−20 min prior to incubation at 37 °C. Duplex samples were 5′end-labeled with γ-[^{31}P] APT (Amersham) using T4 polynucleotide kinase (Roche Diagnostics), as previously described (*17*). Cleavage reaction products were

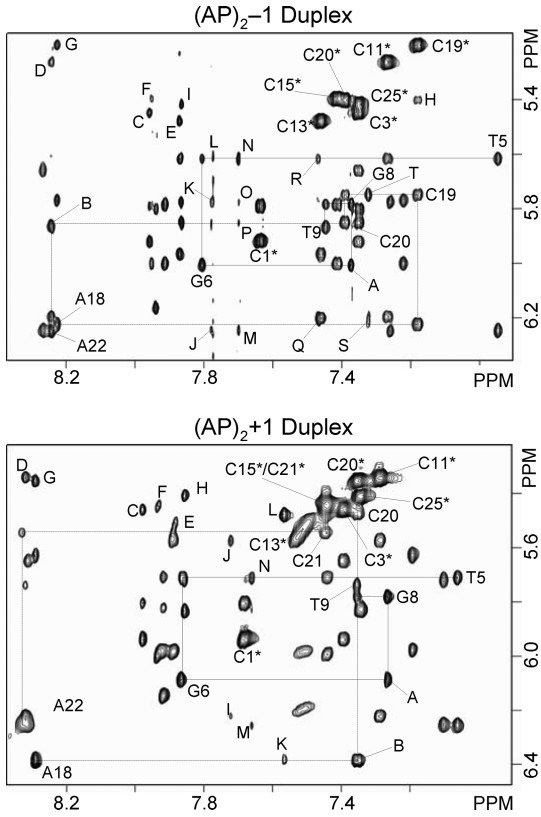

FIGURE 2: Expanded regions of phase sensitive NOESY spectra (300 ms mixing time) recorded at 25 °C with the samples dissolved in D_2O buffer (25 mM Na_2PO_4 and 50 mM NaCl), pH 6.8, showing interactions between the base (7.0−8.4 ppm) and sugar H1′ (5.2−6.5 ppm) protons. Solid lines connect sequential interactions for the (top) $(AP)_2-1$ (bottom) and $(AP)_2+1$ duplexes on the central (...T5-G6-F7-G8-T9...) segment, and broken lines do the same on the complementary strand. Cross-peaks labeled with residue numbers indicate intraresidue base (purine-H8/pyrimidine-H6) to H1′ sugar interactions, and the asterisks denote cytosine H5−H6 cross-peaks. In the $(AP)_2-1$ duplex (top panel), other labels are assigned as follows: A, G8(H8)-G6(H1′); B, A22(H8)-C20(H1′); C, G2(H8)-C3(H5); D, A10(H8)-C11(H5); E, G12(H8)-C13(H5); F, G14(H8)-C15(H5); G, A18(H8)-C19(H5); H, C19(H6)-C20(H5); I, G24(H8)-C25(H5); J, A22(H2)-A22(H1′); K, A22(H2)-T23(H1′); L, A22(H2)-T5(H1′); M, A4(H2)-A4(H1′); N, A4(H2)-T5(H1′); O, A4(H2)-T23(H1′); P, A4(H2)-G24(H1′); Q, A10(H2)-A10(H1′) and C13(H6)-C13(H1′); R, A10(H2)-C11(H1′); S, A18(H2)-A18(H1′) and A18(H2)-A10(H1′); T, A18(H2)-C19(H1′). In the $(AP)_2+1$ duplex (bottom panel), labeled cross-peaks are assigned as follows: A, G8(H8)-G6(H1′); B, C20(H6)-A18(H1′); C, G2(H8)-C3(H5); D, A10(H8)-C11(H5); E G12(H8)-C13(H5); F, G14(H8)-C15(H5); G, A18(H8)-C20(H5); H, G24(H8)-C25(H5); I, A10(H2)-A10(H1′); J, A10(H2)-C11(H1′); K, A18(H2)-A18(H1′); L, A18(H2)-C20(H1′); M, A22(H2)-A22(H1′); N, A22(H2)-T5(H1′).

resolved by 6% SDS−PAGE, visualized, and quantified using a PhosphorImager (Molecular Dynamics Inc.).

RESULTS

Nonexchangeable Proton Spectra of the $(AP)_2-1$ Duplex. NOESY spectra collected for the $(AP)_2-1$ duplex in D_2O buffer are characterized by the presence of sharp signals with few overlapped resonances. Sequence specific assignment of the nonexchangeable protons follows the analysis of two-dimensional NOESY, COSY, and TOCSY spectra collected at room temperature, using standard procedures (*44*−*46*). The top panel of Figure 2 shows an expanded contour map of a NOESY spectrum (300 ms mixing time) depicting interactions between the base (7.0−8.5 ppm) and the sugar H1′ (5.2−6.4 ppm) protons of the $(AP)_2-1$ duplex. Identification of NOE cross-peaks between the pyrimidine H6 (or purine H8) protons and their own and 5′-flanking sugar H1′ protons indicates that the $(AP)_2-1$ duplex is a right-handed helix. Similarly, cross-peaks between cytosine H5 and 5′-flanking base (purine-H8 or pyrimidine-H6) protons (Figure 2, top panel, peaks C−I) and between adenine H2 and sugar H1′ protons on the same and complementary strands (Figure 2, top panel, peaks J-T) are further evidence of the right-handedness of the helix and proper stacking throughout the $(AP)_2-1$ duplex. We observed two sequential NOE cross-peaks, G8(H8)-G6(H1′) and A22(H8)-C20(H1′, between the residues that flank both AP site lesions of the duplex (Figure 2, top panel, peaks A and B), which are consistent with an extra-helical arrangement of both abasic residues in the $(AP)_2-1$ duplex. The complete assignment of the base-sugar H1′ proton region (NOESY walk) is illustrated in Figure 1S (Supporting Information).

NOE cross-peaks between the base (prymidine-H6 or purine-H8) and sugar H2′/2″ protons provide further evidence of the spatial proximity of lesion flanking residues in the $(AP)_2-1$ duplex (Figure 3, top panel). Specifically, a pair of weak cross-peaks between G8(H8)-G6(H2′) and G8(H8)-G6(H2″) indicate the proximity of G8 and G6 residues, which are separated in the duplex sequence by F7 (Figure 3, top panel, peaks D and D′). On the complementary strand, the weak NOE peak between A22(H8)-C20(H2″) indicates proximity of the F21-flanking residues, but no interaction is observed between A22(H8)-C20(H2′) (Figure 3, top panel, peak A and box A′). This is an indication that the abasic residues in the $(AP)_2-1$ duplex are not extruded identically from the helix. The observation of the G6(H8)-G8(H8) and G8(H8)-G6(H3′) NOE peaks (data not shown) between F7 neighboring residues, but not of the corresponding A22(H8)-C20(H6) and A22(H8)-C20(H3′) interactions on the complementary strand, further suggests that the AP residues are differently extruded from the helix in the $(AP)_2-1$ duplex.

The sugar H1′/1″ protons of the AP residues F7 and F21 are readily identified with the aid of COSY spectra by their unique location at 3.9−4.1 ppm but are not stereospecifically assigned (Figure 3S, Supporting Information). These protons show strong COSY interactions with neighboring H2′/2″ protons (Figure 3S (Supporting Information), peaks A and B), which in turn exhibit NOE cross-peaks with their vicinal H3′ protons (Figure 3, top panel, peaks F, F′, and G). Only a few sequential interactions are present between the AP and adjacent residues in the $(AP)_2-1$ duplex suggesting mobility of the AP residues in solution. Weak sequential NOE peaks are observed between G8(H8) and F7(H1′/1″) and F7(H4′) protons, as well as between A22(H8)-F21(H1′/1″) in the complementary strand (data not shown). However, no inter-residue cross-peak is seen between H2′/2″ protons of the AP residues and flanking base protons (Figure 3A). Table 1S (Supporting Information) lists the proton chemical shifts in the $(AP)_2-1$ duplex.

$(AP)_2+1$ Duplex. NOESY spectra collected for the $(AP)_2+1$ duplex in D_2O buffer are also characterized by the presence of sharp signals with few overlapped resonances. As before, the sequence specific assignment of the nonexchangeable protons follows the analysis of two-dimensional NOESY, COSY, and TOCSY spectra, recorded at room

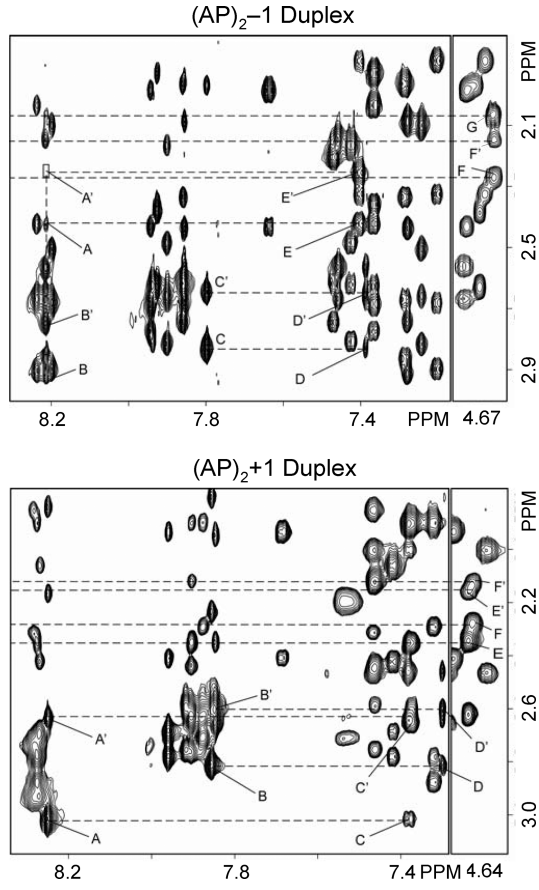

FIGURE 3: Expanded regions of phase sensitive NOESY spectra (300 ms mixing time) recorded at 25 °C with the samples dissolved in D_2O buffer (25 mM Na_2PO_4 and 50 mM NaCl), pH 6.8, showing interactions between the base (7.0−8.4 ppm) and sugar H2′/H2″ (1.8−3.0 ppm) protons in the $(AP)_2-1$ (top) and $(AP)_2+1$ (bottom) duplexes. Labeled peaks are assigned as follows: top panel, A, A22(H8)-C20(H2″); A′, A22(H8)-C20(H2′); B, A22(H8)-A22(H2″); B′, A22(H8)-A22(H2′); C, G6(H8)-G6(H2′); C′, G6(H8)-G6(H2″); D, G8(H8)-G6(H2′); D′, G8(H8)-G6(H2″); E, C20(H6)-C20(H2″); E′, C20(H6)-C20(H2′); F, F21(H3′)-F21(H2″) or F21(H2′); F′, F21(H3′)-F21(H2″) or F21(H2′); and G, F7(H3′)-F7(H2″) and F7(H2′). Bottom panel: A, A18(H8)-A18(H2′); A′, A18(H8)-A18(H2″); B, G6(H8)-G6(H2′); B′, G6(H8)-GG6(H2″); C, C20(H6)-A18(H2″); C′, C20(H6)-A18(H2′); D, G8(H8)-G6(H2′); D′, G8(H8)-G6(H2″); E, F7(H3′)-F7(H2″ or H2′); E′, F7(H3′)-F7(H2″ or H2′); F, F19(H3′)-F19(H2″ or H2′) and F′, F19(H3′)-F19(H2″ or /F19H2′).

temperature, using standard procedures (*44*−*46*). The bottom panel in Figure 2 shows a contour plot of an expanded region of a NOESY spectrum (300 ms mixing time) displaying interactions between the base (7.0−8.5 ppm) and the sugar H1′ (5.2−6.4 ppm) protons of the $(AP)_2+1$ duplex. Cross-peak connectivity between the pyrimidine H6 (or purine H8) protons and their own, and 5′-flanking, sugar H1′ protons indicates that the $(AP)_2+1$ duplex is a right-handed helix in solution. Furthermore, NOE peaks between cytosine H5 and 5′-flanking purine H8 protons (Figure 2, bottom, peaks C to H) and between adenine H2 and sugar H1′ protons (Figure 2, bottom, peaks I to N) are additional evidence of the right-handedness of the helix. As seen in the $(AP)_2-1$ duplex case, strong inter-residue cross-peaks between G8(H8)-G6(H1′), C20(H8)-A18(H1′), and A18(H2)-C20(H1′) (Figure 2, bottom panel, peaks A, B, and L) indicate proximity between the AP flanking residues. These cross-peaks are consistent with an extra helical arrangement of both AP residues in the $(AP)_2+1$ duplex too. The complete NOESY walk is illustrated in Figure 2S (Supporting Information).

NOE peaks between the base (purine H8 and pyrimidine H6) and the sugar H2′/2″ protons offer further evidence of the proximity of lesion flanking residues in the $(AP)_2+1$ duplex (Figure 3, bottom panel). NOE cross-peaks seen between G8(H8)-G6(H2′) and G8(H8)-G6(H2″) and between C20(H6)-A18(H2″) and C20(H6)-A18(H2′) (Figure 3, bottom, peaks D/D′ and C/C′, respectively) indicate the proximity of these residues in the structure and support the extra helical arrangement of F7 and F19 on the $(AP)_2+1$ duplex. Similarly, G6(H8)-G8(H8) and G8(H8)-G6(H3′) NOEs, between the F7 flanking residues, and C20(H6)-A18(H8) and C20(H6)-A18(H3′) interactions, between residues flanking F19 (data not shown), suggest that both AP residues adopt a similar extra helical conformation in the $(AP)_2+1$ duplex. It is interesting to notice that these observations are in contrast to the case of the $(AP)_2-1$ duplex, where only the residues flanking F7 produced those cross-peaks.

Assignment of the F7 and F19 protons follows the identification of the strong H1′/H1″-H2′/H2″ COSY cross-peaks (Figure 4S (Supporting Information), peaks A and B), in a region of the spectrum that lacks other proton interactions. On the NOESY (300 ms mixing time) spectrum of the $(AP)_2+1$ duplex, we observe a pair of cross-peaks in between G8(H8) and F7(H1′/1″) protons and, within the tetrahydrofuran rings, between H3′ and H2′/2″ protons of AP residues, F7 and F21, (Figure 3, bottom, peaks, E, E′, F, and F′). However, as in the case for the $(AP)_2-1$ duplex, there is no inter-residue cross-peak between the H2′/2″ protons of AP residues and any of the flanking base protons (Figure 3). Table 2S (Supporting Information) lists the proton chemical shifts in the $(AP)_2+1$ duplex.

Exchangeable Proton Spectra of the $(AP)_2-1$ Duplex. Figure 4 (left panel) shows the one-dimensional proton spectrum of the $(AP)_2-1$ duplex, recorded in H_2O buffer, pH 6.8, at 5 °C along with an expanded region of a NOESY (220 ms mixing time) spectrum depicting interactions between these and the base/amino protons. At this temperature, seven partially resolved signals account for all imino protons of the duplex, with T(NH3) signals resonating between 13.4−14.0 ppm and G(N1H) peaks appearing between 12.4−13.2 ppm. Sequence specific assignment of the exchangeable protons follows the analysis of the NOESY spectrum recorded under identical conditions. Strong NOE cross-peaks between T(NH3) and A(H2) protons distinguish all four WC A·T pairs of the $(AP)_2-1$ duplex (Figure 4, left panel, peaks A−D). The previous identification of A(H2) protons on the NOESY data collected in D_2O buffer permits the assignment of all T(NH3) signals. Similarly, strong NOE peaks correlate G(N1H) with the hydrogen-bonded and exposed cytosine amino protons across G·C base pairs of the duplex (Figure 4, left panel, peaks E/E′−J/J′). Subsequent identification of intraresidue NOE peaks between the cytosine H5 and NH_2 protons (data not shown) allows the sequence specific assignment of nonterminal C($N4H_2$) signals and, in turn, that of the G(N1H) protons. Notably, the orphan G6 and C20 residues display the NOE interactions that characterize WC alignments (Figure 4, left panel, peaks E−E′), indicating the formation of a canonical G6·C20 base pair at the lesion site of the $(AP)_2-1$ duplex. Furthermore, the observation of sequential NOE interactions between imino

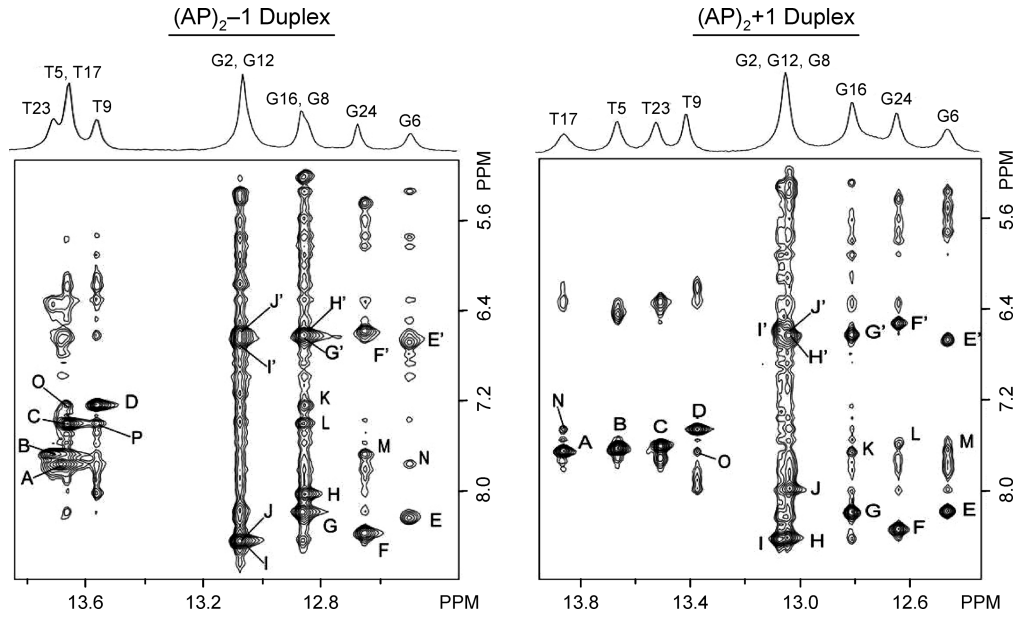

FIGURE 4: Expanded regions of NOESY (220 ms mixing time) spectra recorded at 5 °C in 25 mM phosphate H_2O buffer, pH 6.8, containing 50 mM NaCl and 1.0 mM EDTA. Labeled cross-peaks are assigned as follows: $(AP)_2-1$ duplex, A, T5(N3H)-A22(H2); B, T23(N3H)-A4(H2); C, T17(N3H)-A10(H2); D, T9(N3H)-A18(H2); E/E′, G6(N1H)-C20(N4Hhb)/C20(N4Hex); F/F′, G24(N1H)-C3(N4Hhb)/C3(N4Hex); G/G′, G16(N1H)-C11(N4Hhb)/C11(N4Hex); H/H′, G8(N1H)-C19(N4Hhb)/C19(N4Hex); I/I′, G2(N1H)-C25(N4Hhb)/C25(N4Hex); J/J′ G12(N1H)-C15(N4Hhb)/C15(N4Hex); K, G8(N1H)-A18(H2); L, G16(N1H)-A10(H2); M, G24(N1H)-A4(H2); N, G6(N1H)-A22(H2); O, T17(H3H)-A18(H2) P, T9(N3H)-A10(H2). $(AP)_2+1$ duplex, A, T17(N3H)-A10(H2); B, T5(N3H)-A22(H2); C, T23(N3H)-A4(H2); D, T9(N3H)-A18(H2); E/E′, G6(N1H)-C21(N4Hhb)/C21(N4Hex); F/F′, G24(N1H)-C3(N4Hhb)/C3(N4Hex); G/G′, G16(N1H)-C11(N4Hhb)/C11(N4Hex); H/H′, G2(N1H)-C25(N4Hhb)/C25(N4Hex); I/I′, G12(N1H)-C15(N4Hhb)/C15(N4Hex); J/J′, G8(N1H)-C20(N4Hhb)/ C20(N4Hex); K, G16(N1H)-A10(H2); L, G24(N1H)-A4(H2); M, G6(N1H)-A22(H2); N, T17(N3H)-A18(H2); O, T9(N3H)-A10(H2).

and A(H2) protons (Figure 4, left panel, peaks K−P) and among imino protons of sequential base pairs (Figure 5S, Supporting Information, peaks A−H) suggests proper base pair stacking throughout the $(AP)_2-1$ duplex. Because of their fast solvent exchange, the imino protons of terminal residues fail to show NOE interactions with other DNA protons, and only the observation of exchange cross-peaks with solvent permits their identification on the spectrum. Table 1S (Supporting Information) lists the chemical shifts of the exchangeable proton in the $(AP)_2-1$ duplex.

$(AP)_2+1$ Duplex. The one-dimensional proton spectrum recorded in H_2O buffer, pH 6.8, at 5 °C shows that the imino proton signals of the $(AP)_2+1$ duplex are better resolved than those of the $(AP)_2-1$ cluster (Figure 4, right panel). Sequence specific assignment of these protons follows the analysis of NOESY (140 and 220 ms mixing time) spectra recorded under identical conditions. Strong interactions between T(N3H) and A(H2) protons identify all WC A·T base pairs of the $(AP)_2+1$ duplex (Figure 4, right panel, peaks A-D). Similarly, NOE peaks between G(N1H) and C($N4H_2$) protons (Figure 4, right panel, peaks E/E′−J/J′) permits the assignment of all internal G·C base pairs of the duplex. As was the case of the $(AP)_2-1$ duplex, we observe NOE interactions between orphans G8 and C20 residues (Figure 4, right panel, peaks J/J′) indicating the formation of a canonical G·C base pair at the lesion site of the $(AP)_2+1$ duplex. Sequential NOE interactions between imino and A(H2) protons (Figure 4, left panel, peaks K−O) and among imino protons of sequential base pairs (Figure 5S, Supporting Information, peaks A−I) indicate proper base pair stacking throughout the $(AP)_2+1$ duplex. As before, the imino protons of terminal residues fail to show NOE interactions with other DNA protons, and only the observation of exchange cross-peaks with solvent permits their identification. Table 2S, Supporting Information, lists the chemical shift of the exchangeable protons in the $(AP)_2+1$ duplex.

Thermal Stability. Duplex melting provides a direct assessment of the impact that lesions have on the stability of duplex formation. Analysis of UV_{260} melting curves revealed that both $(AP)_2$ duplexes have similar melting temperature values, which are about 17% lower than that of the unmodified control duplex (data not shown). Figure 5 shows the imino proton region of the one-dimensional spectra of $(AP)_2$ duplexes recorded in H_2O buffer, pH 6.8, in the 5 to 55 °C range. Because of the fast water solvent, the imino proton signals of terminal base pairs in both duplexes are almost undetected, even at low temperature, appearing as a broad shoulder at the base of the overlapping G2(N1H)-G12(N1H) peak (Figure 5). During the transition to random coil, both clusters behave similarly, melting inward from the ends of the duplexes. As the temperature increases, the T5(N3H), G6(N1H), and G8(N1H) signals of the $(AP)_2-1$ duplex are seen on the 40 and 50 °C spectra, indicating the persistence of lesion site T5·A22, G6·C20, and G8·C19 base pairs at high temperature (Figure 5, left panel). In the $(AP)_2+1$ duplex, the G8(N1H) signal overlaps with the G2(N1H)-G12(N1H) peak and, thus, cannot be monitored independently. However, G6(N1H) and T9(N3H) signals are still seen in the 50 °C spectrum, establishing the presence of G6·C21 and T9·A18 base pairs at that temperature and suggesting that G8·C20 may be present as well (Figure 5, right panel). Further temperature increase causes general broadening of the remaining imino proton signals, indicating extensive melting of both $(AP)_2$ duplexes at 55 °C.

Three-Dimensional Structures. Analysis of the rmsd matrix identified a family of distance-refined structures for each duplex that converged with pair wise values <1.5 Å. The refined structures are in good agreement with of the ex-

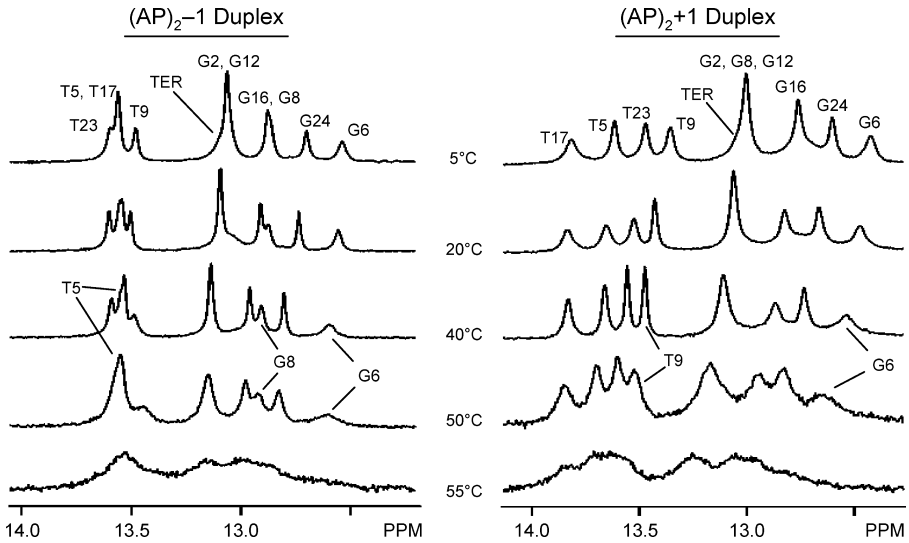

FIGURE 5: Temperature dependence of imino proton signals on the (left) $(AP)_2-1$ and (right) $(AP)_2+1$ duplexes, recorded in 25 mM phosphate buffer, pH 6.8, containing 50 mM NaCl and 1.0 mM EDTA.

Table 1: Molecular Dynamics Statistics[a]

	$(AP)_2-1$ duplex	$(AP)_2+1$ duplex
Covalent Geometry Violations (rmsd)		
bond lengths (Å)	0.02	0.01
bond angles (°)	5	4
improper angles (°)	0.7	0.5
Van der waals Energy (kcal/mol)	−286	−262
Experimental Restraints Violations (rmsd)		
NOE distances (Å) (number of distances)	0.04 (436)	0.02 (441)
constrained dihedrals (°) (number of constrains)	0.3 (216)	0.2 (216)
NMR R-factors (%) (values on initial structures)	13.2 (16.5)	12.8 (16.3)

[a] Averaged values computed from the five converging structures.

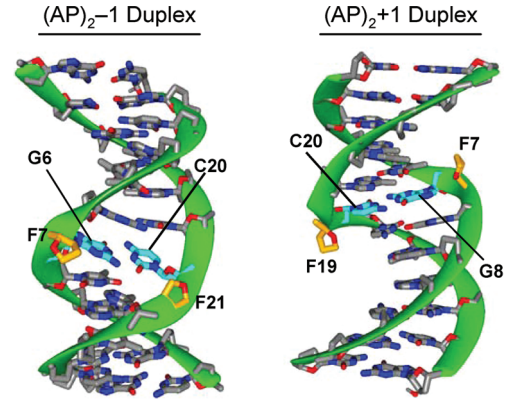

FIGURE 6: Ribbon representations (*49, 50*) of the averaged distance-refined structure shown with the minor groove prominent in the $(AP)_2-1$ duplex and the major groove prominent in the $(AP)_2+1$ duplex. Unmodified nucleotides are colored by atom type and AP residues appear with the O4′ atom in red. In the $(AP)_2-1$ duplex, F7, to a greater extent, and F21 are extruded toward the minor groove. In the $(AP)_2+1$ duplex, both AP residues are similarly extruded into the major groove.

perimental NMR data and have no violation of the NOESY-spectra-derived inter-proton distances >0.1 Å. In addition, back calculation of the NOE intensities using the refined $(AP)_2-1$ and $(AP)_2+1$ duplex structures show the residual factors (NMR R-factors) dropping to about 13.2% and 12.8%, respectively, indicating that the three-dimensional models quantitatively agree with the experimental data. Figures 6S and 7S (Supporting Information) show stereo views of the refined models, and Table 1 lists statistics of the refinement. As shown in Figure 6, the $(AP)_2-1$ and $(AP)_2+1$ duplexes are regular right-handed helices with WC base pair alignments throughout. There is compression at the lesion site of the duplexes, which produces bulged AP sites and shortening of the end-to-end distances by 7% and 5% on the $(AP)_2-1$ and $(AP)_2+1$ duplexes, respectively. The helical axis of both duplexes is bent in the direction of the major groove, 30° in the $(AP)_2-1$ cluster and 15° in the $(AP)_2+1$ cluster, partially contributing to helix shortening. Table 2 summarizes structural parameters of the $(AP)_2$ duplexes.

Figures 7 and 8 show cross-eye stereo views of the $(AP)_2$ duplexes depicting lesion site conformation. In the $(AP)_2-1$ cluster, AP residues are unequally extruded from the helix. F7 forms an abasic bulge, inducing a kink in the sugar−phosphate backbone, while F21 is mostly in line with the backbone, slightly pushing the A22 phosphate toward the solvent (Figure 7). By contrast, F7 and F19 are completely extra helical in the $(AP)_2+1$ duplex, forming similar AP bulges on both strands (Figure 8). A remarkable structural difference between the duplexes is the position of the abasic residues, which appear in the minor grove and are closer to each other in the $(AP)_2-1$ duplex (Figure 7) while they locate in the major groove and are farther apart in the $(AP)_2+1$ duplex (Figure 8). However, since the AP residues are small, groove width and depth dimensions in both duplexes remain, however, unaltered by their presence.

Local structural perturbations are more significant in the $(AP)_2-1$ duplex. Both, G6 and C20 move toward the major groove of the duplex, showing a base pair X-displacement (X-disp) of −0.16 Å as opposed to −0.71 Å in B-form DNA. Mostly G6 and C20, to a lesser extent, are inclined, bringing them to the same plane and allowing the formation of a WC base pair at the lesion site (Figure 7). In addition, they undergo compensatory Y-displacement (Y-disp) facilitating the formation of the G6·C20 base pair. Sugar conformations are somewhat flexible in the $(AP)_2-1$ cluster. G6 and C20 sugars appear in the C3′-exo and C1′-exo conformations,

Table 2: Structural Properties of $(AP)_2$ Duplexes[a]

	$(AP)_2-1$ duplex	$(AP)_2+1$ duplex
Duplex Curvature and Lesion Site Base Parameters		
helix shortening (%)[b]	5.8−8.6	4.6−6.2
helix bend (°)	22−39	10−21
bend direction	major groove	major groove
G6|G8: X-disp (Å), Y-disp (Å), incl (°)	−0.25, +0.22, 15	−3.17, +0.39, 7
C20: X-disp (Å), Y-disp (Å), incl (°)	−0.07, −0.38, −3	−2.51, −0.93, 4
central G•C pair: X-disp (Å), Y-disp (Å), incl (°)	−0.16, 0.30, 9	−2.84, 0.66, 2
Sugar Pucker		
G6|G8	C3′-exo[c]	C2′-endo
C20	C1′-exo[c]	C2′-endo
F7	C2′-exo	C2′-endo[d]
F21|F19	C2′-endo	C2′-endo

[a] Calculated on the refined converging structures using CURVES 5.1 (*38, 39*). [b] Percentage relative to the length of the 13-mer B-form duplex control. [c] One structure in the C2′-endo range. [d] One structure in the C2′-exo range. Normal values in B-form DNA are X-displacement = −0.71 Å; Y-displacement = 0 Å; inclination = 6°.

respectively, in four out of five refined structures, and F7 adopts C2′-exo and F21 C2′-endo puckers in all of the refined models.

In contrast to the $(AP)_2-1$ cluster, structural perturbations at the lesion site of the $(AP)_2+1$ duplex are relatively minor. The lesion site base pair, G8•C20, appears displaced to the minor groove and in the direction of the F7 strand backbone, without changing its inclination value. Furthermore, all lesion site sugars are in the C2′-endo range, with F7 in a C2′-exo conformation in only one of the refined models. Structural parameters at the lesion site of $(AP)_2$ duplexes are summarized in Table 2.

hApe1 Incision of $(AP)_2$ Duplexes. As shown in Figure 9, recombinant Ape1 processes $(AP)_2$ clusters with different efficiency that depended on the lesion orientation within the cluster and their sequence context. The enzyme shows weak incision activity on the $(AP)_2-1$ cluster, cleaving less than 10% of either abasic site under conditions that cleave close to 90% of a control duplex having a single AP site in the F7 sequence context (Figure 9, top panel). Further addition of hApe1 increased the amount of $(AP)_2-1$ incised fractions only slightly, reaching about 35% of the substrate after overnight incubation (data not shown). In contrast, hApe1 exhibits strong activity on the $(AP)_2+1$ cluster, cutting the F7 AP site with efficiency similar to that recorded for the control duplex, while the other AP site (F19) shows a reduced level of cleavage (Figure 9, bottom panel). In addition, after supplementing the reaction with an additional amount of hApe1, overnight incubation shows over 70% incision at F19 (data not shown).

DISCUSSION

NMR Spectra and Solution Structure of $(AP)_2$ Duplexes. The directionality of NOE peaks between base and sugar H1′ protons (Figures 1S and 2S, Supporting Information) and the observation of hydrogen bonded base imino protons (Figure 4) establish that $(AP)_2$ duplexes are right-handed helices stabilized by WC base pairs (*44−46*). There is compression at the damage site of the duplexes pushing the abasic residues out of the helix and bringing the lesion flanking nucleotides close in space (Figure 2, peaks A and B). However, disparities on NOE interactions between base and sugar H2′, H2″, and H3′ protons reveal that the extra helical character of the abasic residues in these duplexes is different. Sequential NOE peaks observed between G6 and G8 in one strand and A18 and C20 in the other strand of the $(AP)_2+1$ duplex are equivalent (Figure 3), indicating that F7 and F19 are extruded from the helix to a similar extent. By contrast, the corresponding interactions between C20 and A22 residues are missing in the $(AP)_2-1$ duplex (Figure 3), suggesting a different extra helical conformation for F21 in the $(AP)_2-1$ cluster. Notwithstanding this difference, lesion counter residues can form a WC G•C base pair in both duplexes (Figure 4), preserving the loss of double stranded character at their lesion site.

Restrained MD reduced the NMR R-factors of the initial $(AP)_2-1$ and $(AP)_2+1$ models to about 20 and 22%, respectively (Table 1), confirming that the refined structures are accurate representations of the experimental NMR data. On both duplexes, the AP residues bulge out appearing in the major groove of the $(AP)_2+1$ cluster (Figures 6 and 8) or in the minor groove of the $(AP)_2-1$ duplex (Figures 6 and 7), where F7 is partially extra helical. The extra helical location of the AP residues in the $(AP)_2+1$ duplex bears striking similarity to the conformation of abasic frame-shift intermediates, where the single AP residue forms a bulge in the major groove of the duplex without perturbing the global DNA conformation (*32, 33*). The structure of bistranded $(AP)_2\pm1$ clusters is also quite different from that of duplexes having a single abasic residue, where both the apyrimidinic site and counter nucleotide are always intra-helical (*19−21, 25−31*), or the apurinic site and sometimes its partner base position outside the helix (*21, 23, 26, 27*). Structurally, then, bistranded $(AP)_2\pm1$ clusters are unique lesions that do not have the characteristics of two single AP sites put together.

In this study, we designed the $(AP)_2\pm1$ duplexes to have one AP residue in each cluster opposite dC and the other opposite dG and established whether the relative orientation of the lesions affected the putative formation of a central G•C base pair. Our results show that while lesion directionality within the cluster determines the groove location of the AP residues, formation of a proper G•C base pair occurs in both cases. Previously, we determined the structures of bistranded $(AP)_2\pm1$ duplexes, having dG and dA as AP site partners. Similar to the structures reported here, there was helix compression in both clusters bringing the orphan purine residues to register with the formation of G•A mismatches. In the +1 orientation, the AP residues bulged out toward the major groove, and the resulting G•A alignment was highly propeller twisted and noncoplanar. In the −1 orientation, however, AP residues remained mostly aligned with the sugar−phosphate backbone, facilitating the formation of a coplanar G•A mismatch. Hydrogen bond interactions were absent in both mismatches (*34*). While many more combinations of orphan bases are possible, it is apparent that helix compression, duplex collapse, and subsequent formation of a base pair at the lesion site is a general structural feature of bistranded $(AP)_2\pm1$ duplexes. The identity of the AP site partners will determine the quality of the lesion site base pair, matched or mismatched, affecting in this way the stability of the damaged duplex. The observation that

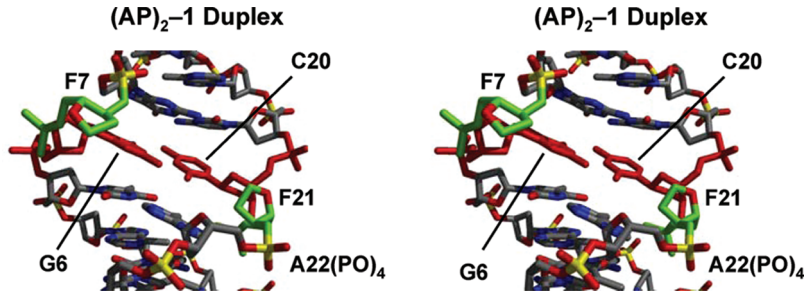

FIGURE 7: Stereo views of the lesion site of the $(AP)_2-1$ duplex seen with the minor groove prominent. AP site atoms are colored in green, the central G·C base pair in red, and other atoms by type.

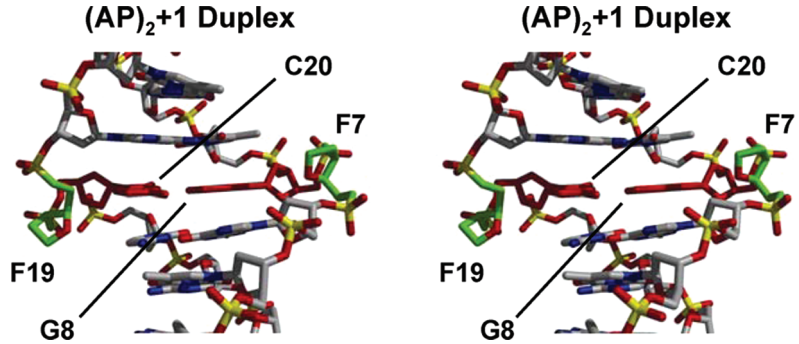

FIGURE 8: Stereo views of the lesion site of the $(AP)_2+1$ duplex seen with the major groove prominent. AP site atoms are colored in green, the central G·C base pair in red, and other atoms by type.

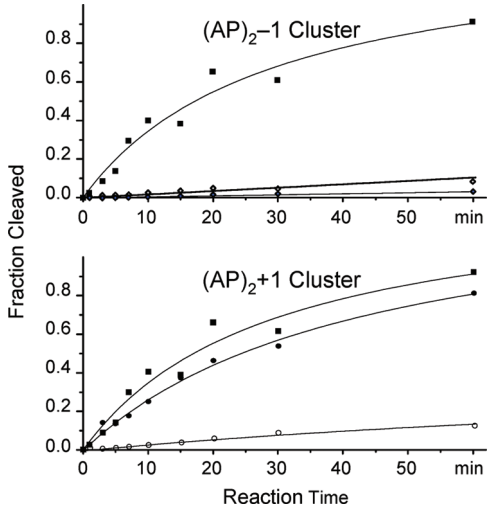

FIGURE 9: Incision of bistranded $(AP)_2 \pm 1$ duplexes by human Ape1 endonuclease. Solid and empty symbols indicate incision at F7 and F19 (or F21), respectively. Solid squares show cleavage of a control duplex sample having a single AP site in the context of the F7 lesion.

following the formation of the central G·C base pair the duplexes have similar melting temperatures (Figure 5) fully supports the concept that orphan residues are main stability determinants on bistranded $(AP)_2\pm1$ clusters. However, cluster orientation will determine the position of the abasic residues, which will be fully bulged out and in the major groove of the duplex for the +1 orientation (Figure 8) or aligned with the backbone, or partially extruded in the minor groove, for the alternative orientation (Figure 7).

Ape1 Processing of $(AP)_2$ Duplexes. Several groups have shown that cleavage of bistranded $(AP)_2$ lesions by recombinant hApe1, or their processing by nuclear cell extracts, is orientation specific such that $(AP)_2+1$ clusters are incised more efficiently than $(AP)_2-1$ lesions (*10*−*17*). In agreement with these reports, we observe here that purified hApe1 preferentially incises AP sites with the +1 orientation, preference that is remarkable in the case of F7, which has identical sequence context in both duplexes (Figure 9). The reasons for this differential processing, however, remain largely unknown. It has been proposed that bistranded abasic site lesions disrupt in general the footprint of hApe1 or that the presence of the second AP lesion hinders specific enzyme−DNA contacts. Alternatively, it was suggested that clustered lesions strongly destabilize the helix, increasing the partial single stranded character of the duplex at the lesion site and, thus, reducing the affinity for hApe1. Without answering all the questions, the results reported here can rule out some of the possibilities.

The lesion site G·C pair and the lesion flanking G·C and A·T base pairs are present in both duplexes (Figure 4), indicating preservation of the double helical character at their lesion site. In addition, the duplex melting temperatures are almost identical (Figure 5), establishing minimal stability differences between these clusters. Therefore, any putative increase of single stranded character at the lesion site of the duplex or thermal stability variations between bistranded $(AP)_2\pm1$ clusters are not the reasons for their differential recognition by hApe1.

The X-ray structure of a damaged DNA/hApe1 complex shows that, upon binding, the enzyme kinks the DNA helix by 35° and extrudes the abasic residue into its preformed active site pocket. Protein residues contact the duplex at both the major and minor grooves, and the insertion of protein loop at the lesion site stabilizes the AP site counter residue that remains intra-helical (*47*, *48*). Molecular modeling shows that, irrespective of its orientation, a second AP site can fit in the structure of the DNA/hApe1 complex without causing relevant atomic clashes (data not shown). Therefore, it is very unlikely that hindrance of specific enzyme−DNA

contacts by bistranded $(AP)_2\pm1$ substrates would account for their differential processing by hApe1.

The different groove location of AP residues in these clusters may partially explain the variations in hApe1 efficiency. The X-ray structure of the hApe1/DNA complex showed several protein−DNA interactions that specifically defined the orientation of the scissile AP residue in the enzyme catalytic pocket. Our structure of the $(AP)_2+1$ duplex shows the AP residues extruded on the major groove in a conformation that is close to that of the hApe1/DNA complex, suggesting that structural changes following the encounter with the enzyme will be small and have low energy barriers. In contrast, minor groove location of abasic residues in the $(AP)_2-1$ duplex is quite far from that on the productive hApe1/DNA complex and will require major structural adjustments to reach the active site of the enzyme and, thus, have higher energy costs. In addition, the abasic residues are more exposed and enzyme accessible in the $(AP)_2+1$ than the $(AP)_2-1$ duplex, favoring the formation of a protein/DNA complex in the former case.

Conclusions. The use of ionizing radiation is a vital strategy in the treatment for various cancers where cell killing is largely the result of DSB induced apoptosis. Abortive repair of clustered lesions can be the source of additional DSB, increasing the lethal action of radiation. Unrepaired clustered damages will induce DNA mutations, increasing the toxicity of ionizing radiation. We solved the structures of bistranded $(AP)_2\pm1$ clusters and confirmed previous measurement of differential cleavage by hApe1. Our results showed that the different groove location of the AP residues most likely explain their differential hApe1 processing, ruling out thermal stability considerations or disruption of specific enzyme/DNA interactions as possible explanations. Ionizing radiation also forms bistranded clusters having nonadjacent lesion and BER enzymes process them with different efficiency. However, it cannot be assumed that these lesions will follow the same structural principles of the $(AP)_2\pm1$ duplex. Thus, additional studies are needed to establish their conformation and understand and the mechanisms responsible for their differential processing.

ACKNOWLEDGMENT

Thanks to Mr. Erich Bremer for providing computer support services and for information that proved helpful in the creation of figures, and to Ms. Cecilia Torres for synthesis and purification of modified oligodeoxynucleotides. Molecular graphics images were produced using the MidasPlus program from the Computer Graphics Laboratory, University of California, San Francisco (supported by NIH RR-01081).

SUPPORTING INFORMATION AVAILABLE

This material is available free of charge via the Internet at http://pubs.acs.org.

REFERENCES

1. Ward, J. F. (1998) DNA damage produced by ionizing radiation in mammalian cells: identities, mechanisms of formation and reparability. *Prog. Nucleic Acids Res. Mol. Biol. 35*, 95–125.
2. Halliwell, B., and Aruoma, O. I. (1991) DNA damage by oxygen derived species: Its mechanism and measurement in mammalian systems. *FEBS Let. 281*, 9–19.
3. Newcomb, T. G. and Loeb, L. A. (2001) Oxidative Damage and Mutagenesis, in *DNA Damage and Repair, Vol. 1: DNA Repair in Higher Eukaryotes* (Nickoloff, J. A., and Hoekstra, M. F., Eds.) pp 65−84, Humana Press Inc, Totowa, NJ.
4. Sutherland, B. M., Bennett, P. V., Sidorkina, O., and Laval, J. (2000) Clustered damages and total lesions induced in DNA by Ionizing radiation: oxidized bases and strand breaks. *Biochemistry 39*, 8026–8031.
5. Sutherland, B. M., Bennett, P. V., Sidorkina, O., and Laval, J. (2000) Clustered damages induced in isolated DNA and human cells by low doses of ionizing radiation. *PNAS U.S.A. 97*, 103–108.
6. David, S. S., and Williams, S. D. (1998) Chemistry of glycosylases and endonucleases involved in base-excision repair. *Chem. Rev. 98*, 1221–1261.
7. Wallace, S. S. (1997) in *Oxidative Stress and the Molecular Biology of Antioxidant Defenses* (Scandalios, J. G., Ed.) pp 49−90, Cold Spring Harbor Laboratory, Cold Spring Harbor, NY.
8. Wilson III, D. M., Engelward, B. P., and Samson, L. (1988) Prokaryotic Base Excision Repair, in *DNA Damage and Repair, Vol 1: DNA Repair in Prokaryotes and Lower Eukaryotes* (Nickoloff, J. A., andHoekstra, M. F., Eds.) pp 29−64, Humana Press, Totowa, NJ.
9. Blaisdell, J. O., and Wallace, S. S. (2001) Abortive base excision repair of radiation-induced clustered DNA lesions in *Escherichia coli*. *PNAS U.S.A. 98*, 7426–7430.
10. Georgakilas, A. G., Bennet, P. V., Wilson III, D. M., and Sutherland, B. M. (2004) Processing of bistranded abasic DNA clusters in γ-irradiated human hematopoetic cells. *Nucleic Acids Res. 32*, 5609–5620.
11. Chaudhury, M. A., and Weinfeld, M. (1997) Reactivity of human apurinic/apyrimidinic endonuclease and *Escherichia coli* exonuclease III with bistranded abasic sites in DNA. *J. Biol. Chem. 272*, 15650–15655.
12. Chaudhury, M. A., and Weinfeld, M. (1995) The action of *Escherichia coli* endonuclease III on multiply damaged sites in DNA. *J. Mol. Biol. 249*, 914–922.
13. Harrison, L., Hatahet, Z., and Wallace, S. S. (1999) *In vitro* repair of synthetic ionizing radiation-induced multiply damaged DNA sites. *J. Mol. Biol. 290*, 667–684.
14. Weinfeld, M., Rasouli-Nia, A., Chaudhury, M. A., and Britten, R. A. (2001) Response of base excision repair enzymes to complex DNA lesions. *Radiat. Res. 156*, 584–589.
15. David-Cordonnier, M.-H., Cunniffe, S. M. T., Hickson, I. D., and O'Neill, P. (2002) Efficiency of incision of an AP site within clustered DNA damage by the major human AP endonucleases. *Biochemistry 41*, 634–642.
16. Lomax, M. E., Cunniffe, S., and O'Neill, P. (2004) Efficiency of repair of an abasic site within DNA clustered damage sites by mammalian cell nuclear extracts. *Biochemistry 43*, 11017–11026.
17. Tian, K., McTigue, M., and de los Santos, C. (2002) Sorting the consequences of ionizing radiation: processing of 8-oxoguanine/abasic site lesions. *DNA Repair 1*, 1039–1049.
18. Wilson, D. M., III, Takeshita, M., Grollman, A. P., and Demple, B. (1995) Incision activity of human apurinic endonuclease (Ape) at abasic site analogs in DNA. *J. Biol. Chem. 270*, 16002–16007.
19. Kalnik, M. W., Chang, C.-N., Grollman, A. P., and Patel, D. J. (1988) NMR studies of abasic sites in DNA duplexes: deoxyadenosine stacks into the helix opposite cyclic analogue of 2′-deoxyribose. *Biochemistry 27*, 924–931.
20. Kalnik, M. W., Chang, C.-N., Johnson, F., Grollman, A. P., and Patel, D. J. (1989) NMR studies of abasic sites in DNA duplexes: deoxyadenosine stacks into the helix opposite acyclic lesions. *Biochemistry 28*, 3373–3383.
21. Cuniasse, Ph., Fazakerley, G. V., Guschlbauer, W., Kaplan, B., and Sowers, L. C. (1990) The abasic site as a challenge to DNA Polymerase. a nuclear magnetic resonance study of G, C, and T opposite a model abasic site. *J. Mol. Biol. 213*, 303–314.
22. Withka, J. M., Wilde, J. A., and Bolton, P. H. (1991) Characterization of conformational features of DNA heteroduplexes containing aldehidic abasic sites. *Biochemistry 30*, 9931–9940.
23. Singh, M. P., Hill, G. C., Péoc'h, D., Rayner, B., Imbach, J.-L., and Lown, J. W. (1994) High-field NMR and restrained molecular modeling studies on a DNA heteroduplex containing a modefied apurinic abasic site in the form of covalently linked 9-aminoellipticine. *Biochemistry 33*, 10271–10285.
24. Goljer, I., Kumar, S., and Bolton, P. H. (1995) Refined solution structure of a DNA heteroduplex containing an aldehydic abasic site. *J. Biol. Chem. 270*, 22980–22987.

25. Wang, K. Y., Parker, S. A., Goljer, I., and Bolton, P. H. (1997) Solution structure of a duplex DNA with an abasic site in a dA tract. *Biochemistry 36*, 11629–11639.
26. Coppel, Y., Berthet, N., Coulombeau, C., Coulombeau, C., Garcia, J., and Lhomme, J. (1997) Solution conformation of an abasic DNA undecamer duplex d(CGCACXCACGC).d(GCGTGTGCG): the unpaired thymine stacks inside the helix. *Biochemistry 36*, 4817–4830.
27. Beger, R. D., and Bolton, P. H. (1998) Structures of Apurinic and Apyrimidinic Sites in Duplex DNAs. *J. Biol. Chem. 273*, 1565–1573.
28. Hoehn, S. T., Turner, C. J., and Stubbe, J. (2001) Solution structure of an oligonucleotide containing an abasic site: evidence for an unusual deoxyribose conformation. *Nucleic Acids Res. 29*, 3413–3423.
29. de los Santos, C., El-khateeb, M., Rege, P., Tian, K., and Johnson, F. (2004) Structural impact of $C_{1'}$(OH) conformation on duplex DNA containing abasic sites. *Biochemistry 43*, 15349–15357.
30. Chen, J., Dupradeau, F. Y., Case, D. A., Turner, C. J., and Stubbe, J. (2007) Nuclear magnetic resonance structural studies and molecular modeling of duplex DNA containing normal and 4′-oxidized abasic sites. *Biochemistry 46*, 3096–3107.
31. Chen, J., Dupradeau, F. Y., Case, D. A., Turner, C. J., and Stubbe, J. (2008) DNA oligonucleotides with A, T, G or C opposite an abasic site: structure and dynamics. *Nucleic Acids Res. 36*, 253–162.
32. Lin, Z., Hung, K.-N., Grollman, A. P., and de los Santos, C. (1998) Solution structure of duplex DNA containing an extrahelical abasic site analog determined by NMR spectroscopy and molecular dynamics. *Nucleic Acid Res. 26*, 2385–2391.
33. Cuniasse, Ph., Sowers, L. C., Eritja, R., Kaplan, B., Goodman, M. F., Cognet, J. A. H., Le Bert, M., Guschlbauer, W., and Fazakerley, G. V. (1989) Abasic frameshift in DNA. Solution conformation determined by proton NMR and molecular mechanics calculations. *Biochemistry 28*, 2018–2026.
34. Lin, Z., and de los Santos, C. (2001) NMR characterization of clustered bistrand abasic site lesions: effect of orientation on their solution structure. *J. Mol. Biol. 308*, 341–352.
35. States, D. J., Haberkorn, R. A., and Ruben, D. J. (1982) A two-dimensional nuclear Overhauser experiment with pure absorption phase in four quadrants. *J. Magn. Reson. 48*, 286–292.
36. Plateau, P., and Gueron, M. (1982) Exchangeable proton NMR without baseline distortion, using new strong-pulse sequences. *J. Am. Chem. Soc. 104*, 7310–7311.
37. Brunger, A. (1993) *X-PLOR*, version 3.1, A System for X-ray Crystallography and NMR, Yale University Press, New Haven, CT.
38. Lavery, R., and Sklenar, H. (1988) The definition of generalized helicoidal parameters and axis of curvature for irregular nucleic acids. *J. Biomol. Struct. Dyn. 6*, 63–91.
39. Lavery, R., and Sklenar, H. (1989) Defining the structure of irregular nucleic acids: conventions and principles. *J. Biomol. Struct. Dyn. 6*, 655–667.
40. Brooks, B., Bruccoleri, R., Olafson, B., States, D., Swaminathan, S., and Karplus, M. (1983) CHARMM: a program for macromolecular energy, minimization, and dynamics calculations. *J. Comput. Chem. 4*, 187–217.
41. Majumdar, A., and Hosur, R. V. (1992) Simulation of 2D NMR spectra for determination of solution conformations of nucleic acids. *Prog. NMR Spectrosc. 24*, 109–158.
42. Rinkel, L. J., and Altona, C. (1987) Conformational analysis of deoxyrybofuranos ring in DNA by means of sums of proton-proton coupling constants: a graphical method. *J. Biomol. Struct. Dyn. 4*, 621–649.
43. Ryckert, J.-P., Ciccoti, G., and Berendsen, H. J. C. (1977) Numerical integration of Cartesian equations of motion of a system with constraints-molecular-dynamics of N-alkanes. *J. Comput. Phys. 23*, 327–341.
44. van de Ven., F. J., and Hilbers, C. W. (1988) Nucleic acids and nuclear magnetic resonance. *Eur. J. Biochem. 178*, 1–38.
45. de los Santos, C. (1999) Probing DNA Structure by NMR Spectroscopy, in *Comprehensive Natural Products Chemistry, Vol. 7: DNA and Aspects of Molecular Biology* (Kool, E., Barton, D., Nakanishi, K., and Meth-Cohn, O., Eds.) pp 55−80, Elsevier Science Ltd., Oxford, UK.
46. Hare, D. R., Wemmer, D. E., Chou, S. H., Drobny, G., and Reid, B. (1983) Assignment of the non-exchangeable proton resonances of d(C-G-C-G-A-A-T-T-C-G-C-G) using two-dimensional nuclear magnetic resonance methods. *J. Mol. Biol. 171*, 319–336.
47. Gorman, M. A., Morera, S., Rothwell, D. G., de La Fortelle, E., Mol, C. D., Tainer, J. A., Hickson, I. D., and Freemont, P. S. (1997) The crystal structure of the human DNA repair endonuclease HAPE1 suggests the recognition of extra-helical deoxyribose at DNA abasic sites. *EMBO J. 16*, 6548–6558.
48. Mol, C. D., Izuml, T., Mitra, S., and Tainer, J. A. (2000) DNA-bound structures and mutants reveal abasic DNA binding by APE1 DNA repair and coordination. *Nature 403*, 451–456.
49. Ferrin, T. E., Huang, C. C., Jarvis, L. E., and Lngridge, R. (1988) The MIDAS display system. *J. Mol. Graphics 6*, 13–27.
50. Huang, C. C., Pettersen, T. E., Ferrin, T. E., and Lngridge, R. (1991) Conic: A faster render for space-filling molecules with shadows. *J. Mol. Graphics 9*, 230–236.

BI800950T